Molecular Therapy
Methods & Clinical Development
Original Article

Systemic Delivery of AAV-*Fdxr* Mitigates the Phenotypes of Mitochondrial Disorders in *Fdxr* Mutant Mice

Li Yang,[1,2] Jesse Slone,[1] Weiwei Zou,[1,3] Luis F. Queme,[4] Michael P. Jankowski,[4] Fei Yin,[2] and Taosheng Huang[1]

[1]Division of Human Genetics, Cincinnati Children's Hospital Medical Center, Cincinnati, OH 45229, USA; [2]Department of Pediatrics, Xiangya Hospital, Central South University, Changsha, Hunan 410008, China; [3]Reproductive Medicine Center, Department of Obstetrics and Gynecology, The First Affiliated Hospital of Anhui Medical University, Hefei 230022, China; [4]Division of Anesthesia, Cincinnati Children's Hospital Medical Center, Cincinnati, OH 45229, USA

Gene therapy now provides a novel approach for treating inherited monogenetic disorders, including nuclear gene mutations associated with mitochondrial diseases. In this study, we have utilized a mouse model carrying a p.Arg389Gln mutation of the mitochondrial *Ferredoxin Reductase* gene (*Fdxr*) and treated them with neurotropic AAV-PHP.B vector loaded with the mouse *Fdxr* cDNA sequence. We then used immunofluorescence staining and western blot to test the transduction efficiency of this vector. Toluidine blue staining and electronic microscopy were also utilized to assess the morphology of optic and sciatic nerves, and the mitochondrial respiratory chain activity was determined as well. The AAV vector effectively transduced in the central nervous system and peripheral organs, and AAV-*Fdxr* treatment reversed almost all the symptoms of the mutants (*Fdxr*$^{R389Q/R389Q}$). This therapy also improved the electronic conductivity of the sciatic nerves, prevented optic atrophy, improved mobility, and restored mitochondrial complex function. Most notably, the sensory neuropathy, neurodegeneration, and chronic neuroinflammation in the brain were alleviated. Overall, we present the first demonstration of a potential definitive treatment that significantly improves optic and sciatic nerve atrophy, sensory neuropathy, and mitochondrial dysfunction in *FDXR*-related mitochondriopathy. Our study provides substantial support for the translation of AAV-based *Fdxr* gene therapy into clinical applications.

INTRODUCTION

Ferredoxin reductase (FDXR), also known as adrenodoxin reductase, was first isolated from the bovine adrenal cortex as the first enzyme in the mitochondrial P450 system, which catalyzes the necessary steps of steroid hormone biosynthesis.[1] FDXR is an essential component of both the mitochondrial iron-sulfur assembly pathway and mitochondrial respiratory chain complex assembly factors.[2,3] Our group was one of the first to identify the pathogenicity of FDXR mutations in humans and also analyzed the phenotype of a mouse model with a spontaneous *FDXR* mutation. Homozygous and compound heterozygous mutations of *FDXR* lead to a deficiency in the iron-sulfur cluster (ISC)-containing enzymes, reduced levels of heme oxygenase, iron overload in energy-intensive tissues, and a decrease in mitochondrial complex activity. These deficiencies eventually lead to auditory neuropathy, optic atrophy, neurodegeneration associated with inflammation, and movement disorders in both humans and mice.[4–6]

Mutation of *FDXR* can lead to a lethal mitochondrial neuropathy. Six out of fourteen pediatric patients died prematurely in the cohort we reported.[4,6] For most mitochondrial neuropathies, there is no conventional treatment effective enough to counter the pathogenicity of this class of diseases. The most common clinical approach to treat these diseases is the "mitochondrial cocktail," which is merely a combination of vitamins, energetic and metabolic enhancers, and nutritional supplements.[7,8] Some clinical responses have been observed during the process of the "mitochondrial cocktail" treatment.[9] However, none of these therapies genuinely alter the course of the disease. Thanks to the technological advance of next-generation sequencing, more and more mitochondrial diseases have been linked to monogenic mutations in the nuclear genome, as well as to mutations in the mitochondrial genome. Consequently, the mitochondrial neuropathy caused by these mutations could theoretically be cured if the relevant mutation in the nuclear genome could be corrected. The development of adeno-associated virus (AAV) provides the means to effect such a correction by proving a suitable vector to deliver the corrected gene *in vivo*,[10,11] thus offering the potential to cure a broad range of mitochondrial diseases caused by a monogenic mutation in the nuclear genome.

One barrier to this potential approach is how to deliver the corrected gene systematically to the whole body, while also permitting expression in the central nervous system (CNS), which is often particularly hard-hit by the consequences of mitochondrial deficiency. AAV-PHP.B is a recently developed AAV capsid, based on the AAV9 serotype, which has been shown to effectively deliver its genome across the blood-brain barrier and into the CNS in both neonate and adult mice.[12,13] The low antigenicity and excellent safety profile associated with AAV make it a

Received 6 February 2020; accepted 19 May 2020;
https://doi.org/10.1016/j.omtm.2020.05.021.

Correspondence: Taosheng Huang, Division of Human Genetics, Cincinnati Children's Hospital Medical Center, Cincinnati, OH 45229, USA.
E-mail: taosheng.huang@cchmc.org

plausible tool for gene therapy. However, a limitation of this viral vector is that the size of its genome cargo is relatively small; after the inclusion of promoters, reporters, and selection markers, the maximum size available for packaging therapeutic genes into AAV vectors is generally limited to less than 2.4 kb. The size of the full mouse *Fdxr* gene is approximately 9.0 kb,[14] which makes it impossible to be included in the AAV vector. Thus, we subcloned the coding sequence (CDS) of mouse *Fdxr* (1.485 kb; MGI:104724) into an AAV-PHP.B vector, along with the ubiquitous cytomegalic virus promoter (CMV), and delivered it into our previously reported *Fdxr*$^{R389Q/R389Q}$ mouse model. This "AAV-*Fdxr*" vector reversed the majority of the phenotypes of the *Fdxr*$^{R389Q/R389Q}$ mutants, ameliorated their sensory and auditory neuropathy, and helped the mutants regain their motor ability. The results of this study indicate that gene therapy using the AAV-PHP.B vector could be a powerful approach for treating FDXR-related mitochondriopathy and other mitochondrial genetic disorders.

RESULTS

AAV-PHP.B Successfully Delivers *Fdxr* into the CNS and Peripheral Tissues with a Long-Term Expression Pattern

To test the transduction efficiency of AAV-PHP.B in the B6/129S background, we administrated 2×10^{11} genomic copies of AAV-PHP.B-GFP into P2 neonatal *Fdxr*$^{R389Q/R389Q}$ mutants. Both the mice injected with AAV-PHP.B-GFP and the uninjected mice were sacrificed at 2 weeks post-injection. Immunofluorescence (IF) staining showed the ubiquitous distribution of GFP signals in both the cerebral cortex, cerebellum, heart, liver, eyes, and sciatic nerve. Those results confirmed the tropism of AAV-PHP.B in the CNS and peripheral organs (Figure 1A). To test the sustainability of the transgenic product *in vivo*, we performed western blot to detect Fdxr protein inside the brain and adrenal gland of each group of 5-month-old mice. Immunoblotting showed that the Fdxr protein had a similar expression level between wild-type (WT), *Fdxr*$^{R389Q/R389Q}$ mutants, and AAV-treated mutants (Figures 1B and 1D). However, we found a significant discrepancy in FDXR expression in the adrenal gland, which is the tissue with the highest expression under ordinary conditions (Figures 1C and 1E). Compared to *Fdxr*$^{R389Q/R389Q}$ mutants, both the WT mice and the AAV-treated mutants had higher expression within the adrenal gland (WT versus *Fdxr*$^{R389Q/R389Q}$, $p = 0.0027$; AAV-treated versus *Fdxr*$^{R389Q/R389Q}$, $p = 0.038$) and liver (WT versus *Fdxr*$^{R389Q/R389Q}$, $p = 0.0121$; AAV treated versus *Fdxr*$^{R389Q/R389Q}$, $p = 0.0935$). These results indicate that the AAV-PHP.B-*Fdxr* vector delivered sufficient amounts of the therapeutic transgenic product, and the product maintained a significant level of expression over time.

AAV-*Fdxr* Alleviates Neuronal Gliosis and Neurodegeneration in the CNS of *Fdxr*$^{R389Q/R389Q}$ Mutants

Fdxr$^{R389Q/R389Q}$ mice show a phenotype of compromised cognitive ability, as evidenced by their tendency to fail in finding the correct route to escape from the Morris Water maze (MWM). Additionally, the spasticity in the hind limbs and ataxia they present tends to deteriorate over time, leading to substantial difficulty in movement. Therefore, we stained the brain sections of 5-month-old WT mice, untreated *Fdxr*$^{R389Q/R389Q}$ mutants, and *Fdxr*$^{R389Q/R389Q}$ mutants treated with AAV-*Fdxr* with glial fibrillary acidic protein (GFAP) IF staining and Fluoro-Jade C staining to check the status of neuronal gliosis and neurodegeneration in those mice. Enhanced GFAP signals were detected in the cerebellum, hippocampus, and midbrain of *Fdxr*$^{R389Q/R389Q}$ mice, which indicates the presence of enhanced gliosis (Figure 2A). Meanwhile, the GFAP intensity was reduced in the above positions for AAV-*Fdxr* treated mutants. Intensive signals of Fluoro-Jade C were also observed in the hippocampus, cerebellum, and cerebral cortex of *Fdxr*$^{R389Q/R389Q}$ mutants, while the WT controls and the AAV-*Fdxr* treated mutants showed substantially reduced levels of neurodegenerative signal (Figure 2B). Thus, the AAV-*Fdxr* treatment showed a considerable improvement in terms of neuronal gliosis and neurodegeneration relative to the *Fdxr*$^{R389Q/R389Q}$ mutants.

AAV-*Fdxr* Mitigates the Optic Atrophy of *Fdxr*$^{R389Q/R389Q}$ Mutants

To investigate the status of optic atrophy after the gene replacement therapy, we performed H&E staining of eye sections to check the retinal ganglion cell (RGC) layer of 4-month-old males. We found that the loss of cell density in the RGC layer was restored after the AAV treatment (Figure 3A). Compared to untreated mutants, AAV-*Fdxr* treated mutants showed denser nuclear arrangements in the RGC layer (Figure 3E, $p = 0.0067$). We also utilized a cell-specific marker, Brn3a, to visualize RGCs under a confocal fluorescence microscope. IF staining showed recovered signals in the RGC layer after AAV-*Fdxr* treatment (Figures 3B and 3F, $p = 0.0097$). To further explore the morphology of the optic nerves, we performed toluidine blue staining of the optic nerves isolated from those mice. The semi-thin sections indicated no significant difference between each group (Figure 3C). However, electron microscopy (EM) images showed that the axon loss in *Fdxr*$^{R389Q/R389Q}$ mutants (middle panel) was alleviated after AAV-*Fdxr* treatment (Figures 3D and 3G; *Fdxr*$^{R389Q/R389Q}$ versus WT, $p < 0.0001$; *Fdxr*$^{R389Q/R389Q}$ mutants versus AAV-treated mutants, $p = 0.0244$).

AAV-*Fdxr* Mitigates the Peripheral Neuropathy in the Hindlimbs of *Fdxr*$^{R389Q/R389Q}$ Mutants

To examine the electrophysiological status of the sciatic nerve of *Fdxr*$^{R389Q/R389Q}$ mutants after AAV treatment, we conducted electromyography (EMG) on 4-month-old males (Figure 4A). There was no significant difference in maximum amplitude between each group (Figure 4B). Nevertheless, the impaired conduction velocity (CV) of the sciatic nerves of *Fdxr*$^{R389Q/R389Q}$ mutants was restored after AAV treatment (Figure 4C; *Fdxr*$^{R389Q/R389Q}$ versus WT, $p = 0.0002$; *Fdxr*$^{R389Q/R389Q}$ mutants versus AAV-treated mutants, $p = 0.0097$.) Semi-thin toluidine blue staining of the sciatic nerve was also conducted to investigate the morphology of axons of the sciatic nerve after AAV treatment (Figure 4D). We found that axons with irregular shapes were ubiquitous inside the sciatic nerve of *Fdxr*$^{R389Q/R389Q}$ mutants, while it was rarely seen within the axons of WT mice, as well as the axons of mutants who received the AAV treatment. To further explore the micro-structure of the axons of the sciatic nerve, we performed EM on the sciatic nerves of those subjects. Ubiquitous demyelination was evident inside the sciatic nerve of *Fdxr*$^{R389Q/R389Q}$

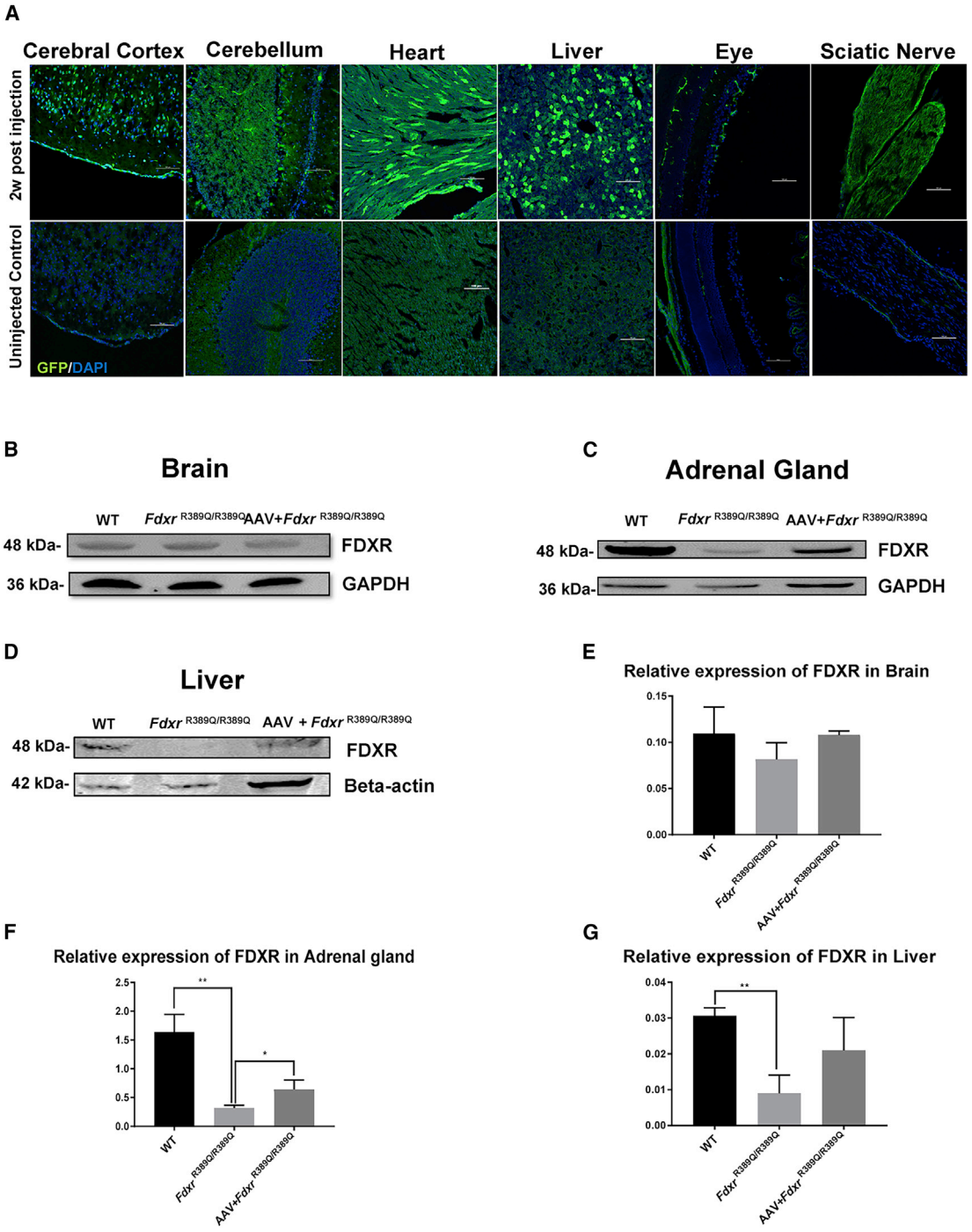

Figure 1. AAV-PHP.B Transduction in the Central Nervous System (CNS) and Peripheral Systems after Administration via Facial Vein Injection

(A) Distribution of GFP reporter expression in the CNS and peripheral tissues. Scale bar, 100 μm. (B) FDXR expression in the brain lysate of 5-month-old mice. (C) FDXR expression in the adrenal gland of 5-month-old mice. (D) FDXR expression in the liver of 5-month-old mice. (E–G) Relative expression of FDXR in the brain (E), adrenal gland (F), and liver (G) lysates. Values are normalized to GAPDH (for brain and adrenal gland) or beta-actin (for liver) as internal controls.

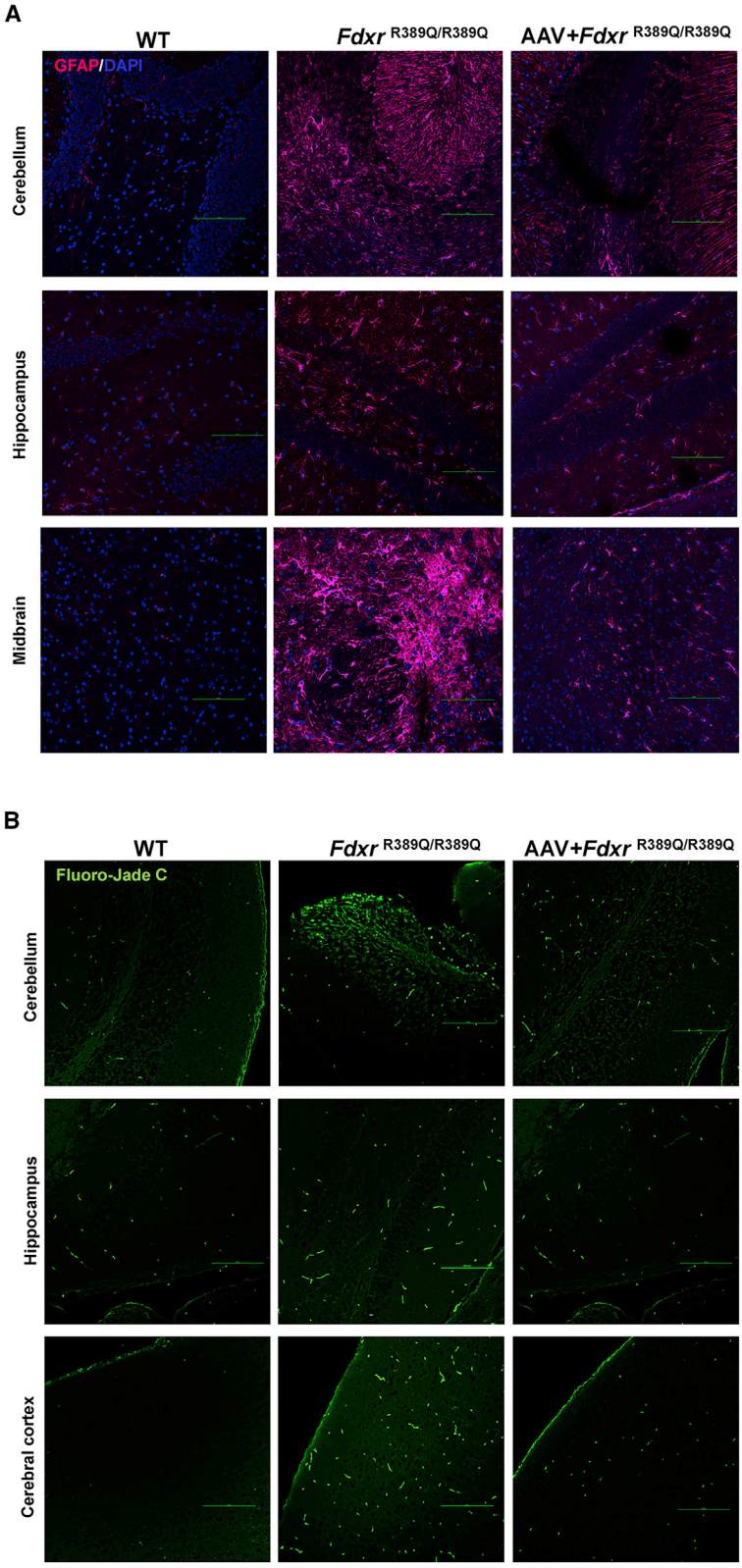

Figure 2. The AAV-*Fdxr* Treatment Alleviates the Neuronal Gliosis and Neurodegeneration in the CNS of *Fdxr*$^{R389Q/R389Q}$ Mutants

(A) Immunofluorescence (IF) with GFAP staining in the mouse cerebellum. Scale bars, 100 μm. Nuclei were counterstained with 4′,6-diamidino-2-phenylindole (DAPI). (B) Fluoro-Jade C staining of Purkinje cells in the mouse brain. The green signal indicates degenerating neurons. Scale bars, 100 μm.

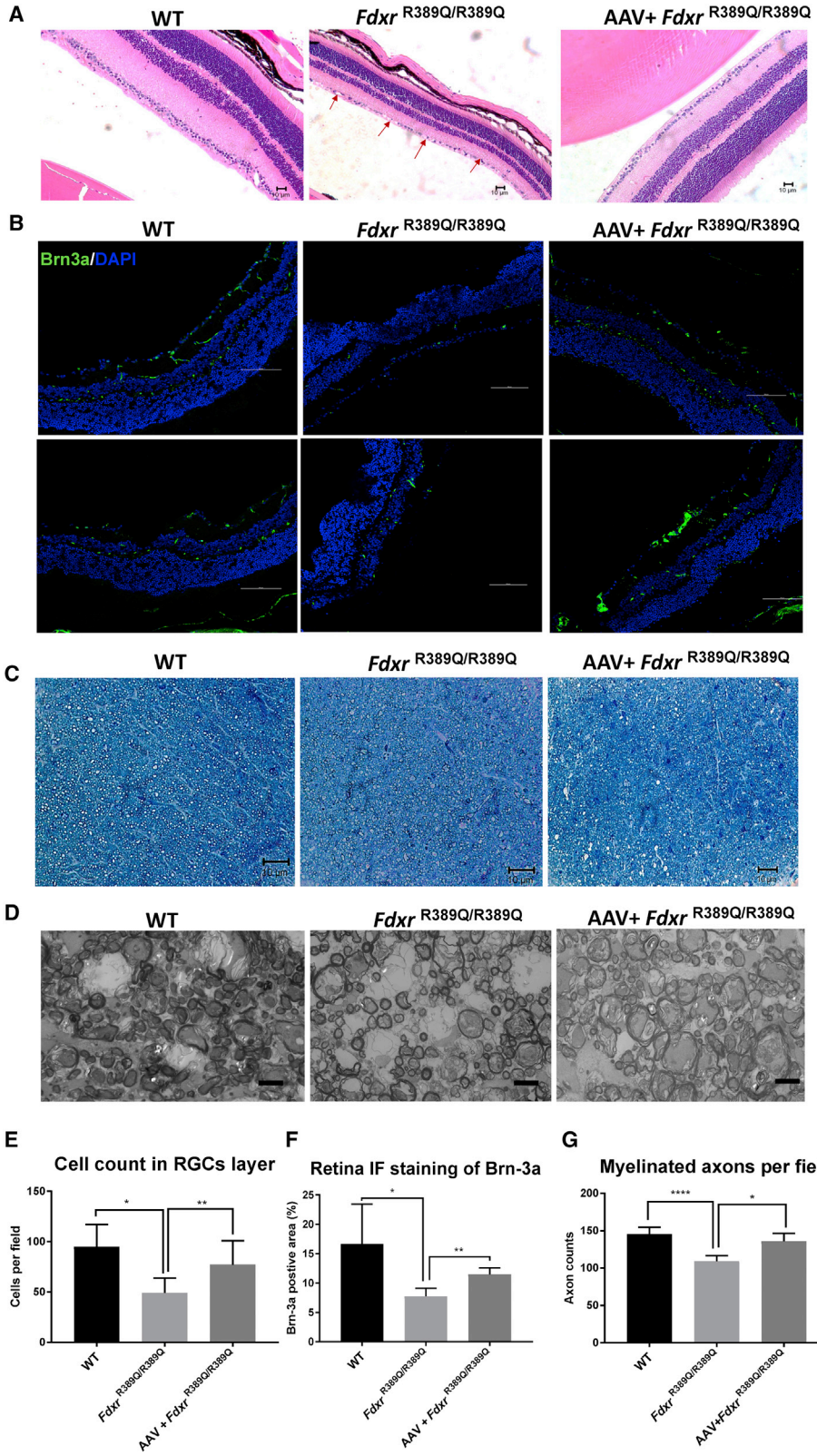

(legend on next page)

mutants under EM, while both WT and the AAV-treated mutants showed more regular shapes (Figures 4E and 4F). When comparing myelinated axons inside the sciatic nerve of each group, *Fdxr*$^{R389Q/R389Q}$ mutants showed a significant deficiency in axon myelination (WT versus *Fdxr*$^{R389Q/R389Q}$, p = 0.0003; *Fdxr*$^{R389Q/R389Q}$ mutants versus AAV-treated mutants, p = 0.0002; Figure 4G). Furthermore, in myelinated axons, analysis of the G-ratio showed a decrease in myelin thickness in *Fdxr*$^{R389Q/R389Q}$ mutants, which was subsequently recovered after AAV treatment. (*Fdxr*$^{R389Q/R389Q}$ versus WT, p < 0.0001; *Fdxr*$^{R389Q/R389Q}$ mutants versus AAV-treated mutants, p < 0.0001).

AAV-*Fdxr* Relieves the Dysfunction of the Mitochondrial Respiratory Chain

In order to estimate the treatment efficacy, the enzyme activities of the mitochondrial complexes of the respiratory chain were measured. The deficiencies of complex I in the brain, heart, and muscle tissues of the *Fdxr*$^{R389Q/R389Q}$ mutants were all significantly recovered after the AAV treatment (Figure 5A, untreated mutant versus AAV-treated mutant brain tissues, p = 0.0907; untreated mutant versus AAV-treated mutant heart tissues, p = 0.0033; untreated mutant versus AAV-treated mutant muscle tissues, p = 0.0212). There was no substantial difference in the activity of complex II+III between each group (Figure 5B). However, after the AAV treatment, the *Fdxr*$^{R389Q/R389Q}$ mutants regained the enzymatic activity of complex IV in the brain and muscle tissues (Figure 5C, WT versus *Fdxr*$^{R389Q/R389Q}$ brain tissues, p = 0.0006; for *Fdxr*$^{R389Q/R389Q}$ versus AAV+*Fdxr*$^{R389Q/R389Q}$ brain tissues, p = 0.0020; for the comparison of muscle tissues, WT versus *Fdxr*$^{R389Q/R389Q}$, p = 0.0013; for *Fdxr*$^{R389Q/R389Q}$ versus AAV+*Fdxr*$^{R389Q/R389Q}$, p < 0.0001).

AAV-*Fdxr* Eliminates the Mitochondrial Iron Overload in Various Tissues of *Fdxr*$^{R389Q/R389Q}$ Mutants

Since FDXR deficiency could lead to iron overload,[15] we tested the mitochondrial iron concentration of different energy-intensive tissues, including the brain, heart, liver, and muscle in 4-month-old male mice. A colorimetric assay for detecting ferric iron showed that the *Fdxr*$^{R389Q/R389Q}$ mutants re-acquired iron homeostasis in heart and muscle after AAV treatment (Figures 6B and 6D, p < 0.0001 for all comparisons).

AAV-*Fdxr* Treatment Reduces the Movement Disorders and Sensory Neuropathy of *Fdxr*$^{R389Q/R389Q}$ Mutants

Since motor ability was severely compromised in both the *FDXR* patients and the *Fdxr*$^{R389Q/R389Q}$ mice,[4] we observed the mutants after treatment to see whether their motion ability was improved after the AAV-*Fdxr* treatment. At first glance, it was clear that the movement difficulty was significantly reduced in the AAV-treated mice (Video S1). To quantify the extent of improvement of motor ability and the sensory neuronal function of the treated mice, we conducted behavioral tests, including measurements of locomotor activities, rotarod, MWM, and the acoustic and tactile startle tests to assess the movement ability of *Fdxr*$^{R389Q/R389Q}$ mutants after AAV treatment. The treated mutants demonstrated a dramatically improved locomotor activity (Figures 7A and 7B, p < 0.0001) and durability on the rotarod (Figures 7C and 7D, p < 0.0001). Furthermore, the AAV-treated mutants had significantly elevated amplitudes in response to both acoustic and tactile stimuli, indicating that they gained better tactile and auditory sensation after the AAV-*Fdxr* treatment (Figures 7E and 7F, p < 0.0001). Moreover, during the MWM experiment, the untreated *Fdxr*$^{R389Q/R389Q}$ mutants were only able to escape 1 time out of a total of 20 trials, while the mutants who received the AAV treatment successfully escaped in 19 out of a total of 20 trials (Figure 7G, p < 0.0001).

DISCUSSION

Although the current "mitochondrial cocktail" treatment has offered some improvements to a portion of patients with mitochondrial disease,[16–19] there is still no cure. The majority of the genes encoding the mitochondrial proteome are in the nuclear genome and align with the rules of Mendelian inheritance.[20] Since the advent of whole exome sequencing (WES), over 250 mitochondrial gene mutations coded by the nuclear genome have been identified.[21] Since a large number of nuclear genes are required for mitochondrial structure and function,[22] nuclear gene mutations are common in pediatric patients, with a prevalence of approximately 1 in 4,300.[23] Mitochondrial disorders are often multisystemic, and seeking efficacious treatments for a large number of untreated rare genetic diseases (including mitochondrial disorders) remains a significant challenge. New advancements in developing therapeutic tools against mitochondrial diseases should thus be attempted and pursued. Each genetic disease has its unique features, and the efficacy of new therapeutic approaches needs to be tested to support clinical success. Herein, we report the correction of the pathogenicity of an *Fdxr* mutation using an AAV-PHP.B vector based on our previously reported mouse model with a homozygous *Fdxr*$^{R389Q/R389Q}$ mutation that recapitulates the clinical features of patients with *FDXR* mutation.

The pathogenic progression of *FDXR* mutation causes dysfunction of multiple systems including the CNS. Optic atrophy, ataxia, hypotonia, seizures, global developmental delay, spasticity and respiratory failure, abnormal movements, and hearing loss have all been reported

Figure 3. AAV-*Fdxr* Mitigates the Optic Atrophy of *Fdxr*$^{R389Q/R389Q}$ Mutants

(A) H&E staining of 4-month-old mouse retinas. Scale bar, 10 μm. Red arrows indicate cell loss in the retinal ganglion cell (RGC) layer of *Fdxr*$^{R389Q/R389Q}$ mutants. (B) Brn3a IF staining of retinas from 4-month-old mice. Scale bar, 100 μm. The middle panel indicates the decrease in Brn3a positive signal in the RGC layer of the *Fdxr*$^{R389Q/R389Q}$ mutant. The right panel shows that the reduction in Brn3a positive cells was reversed after AAV-*Fdxr* treatment. (C) Toluidine blue staining of semi-thin cross-sections of optic nerves from 4-month-old mice. Scale bar, 10 μm. (D) EM cross-sections of optic nerves from 4-month-old mice. Scale bar, 2 μm. Note the axon loss in the middle panel for the *Fdxr*$^{R389Q/R389Q}$ mutant. (E) Cell counts in the RGC layer. (F) Quantification of the Brn3a–positive area in the retinas of 4 month-old mice. Brn3a signals were quantified from six retinal sections. (G) Quantification of myelinated axons from 4-month-old mice.

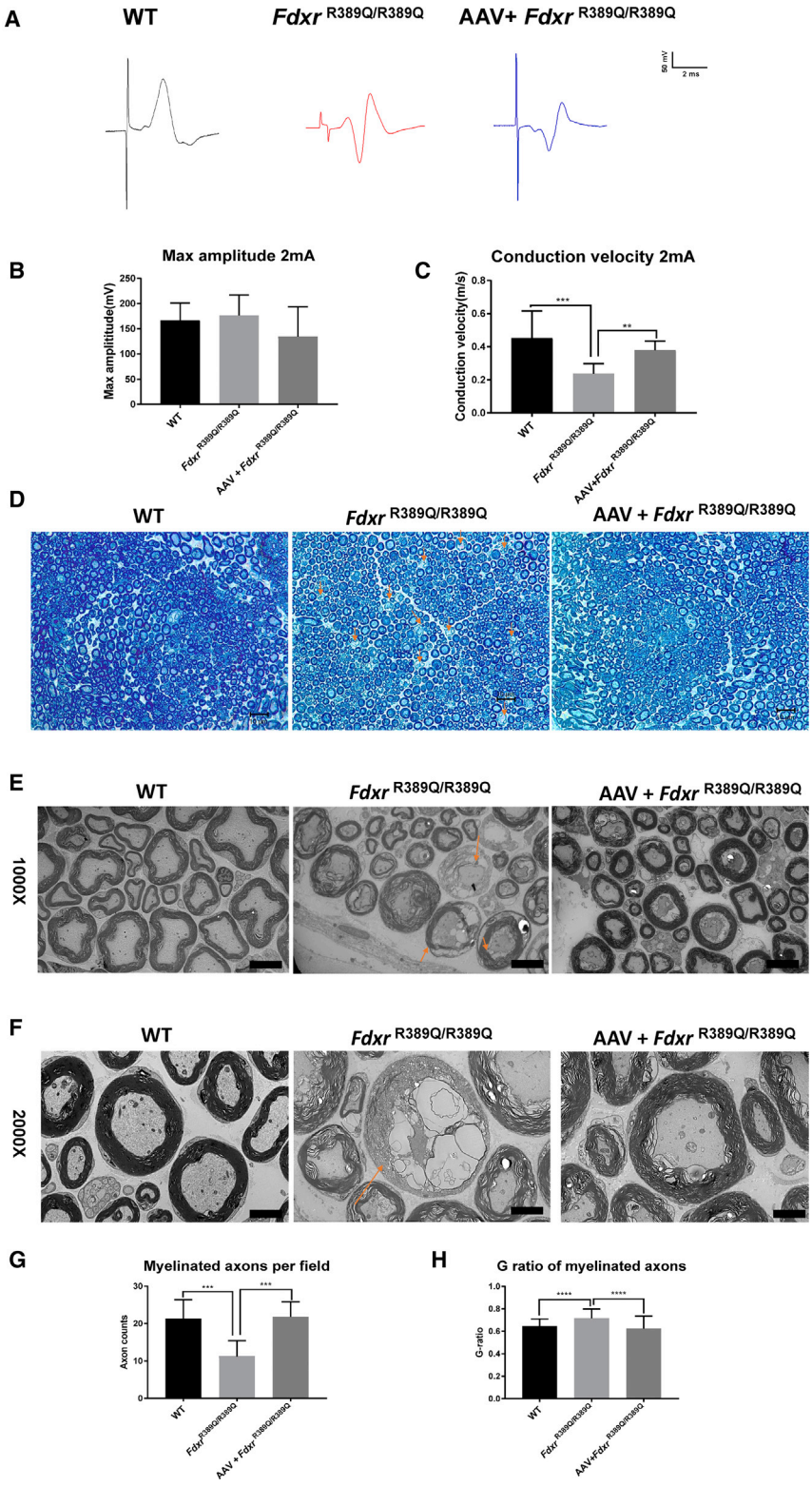

Figure 4. AAV-*Fdxr* Mitigates the Peripheral Neuropathy in the Hindlimbs of *Fdxr*$^{R389Q/R389Q}$ Mutants

(A) Schematic diagram of EMGs recorded from 4-month-old mice. Scales indicate volts and time. (B and C) The maximum amplitude (B) and conduction velocity (C) of 4-month-old mice were compared between each group. (D) Toluidine blue staining of cross-sections from 4-month-old mice. Orange arrows indicate axons undergo demyelination. Scale bar, 10 μm. (E) 1,000× magnification EM images of sciatic nerve cross-sections of 4-month-old mice. Note the demyelinating axons indicated by red arrows. (F) 2,000× magnification EM images of a cross-section of sciatic nerves from 4-month-old mice. Note the disintegrated axon in the middle panel. (G) Comparison of myelinated axons inside the sciatic nerves of each group. Values were obtained from 6 images from each group. (H) G-ratio of myelinated axons inside the sciatic nerves of each group. Values of G-ratio were obtained from 65 random axons from each group.

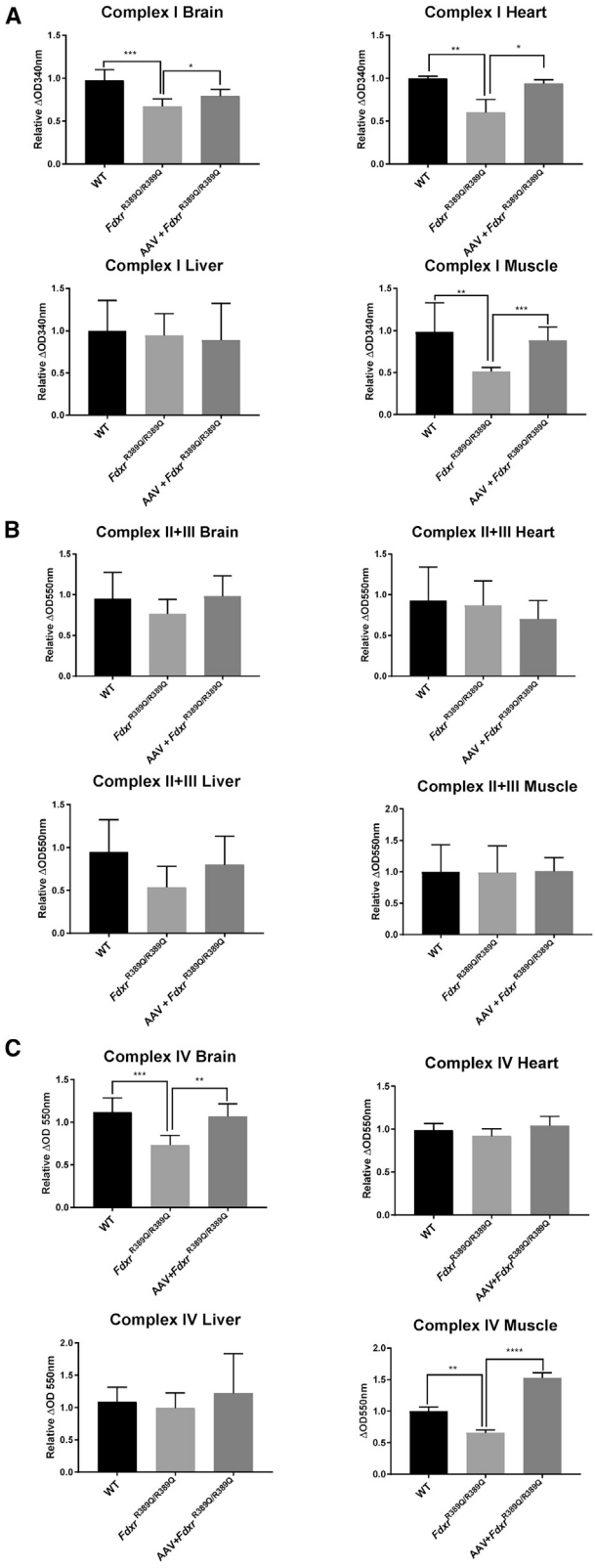

Figure 5. AAV-*Fdxr* Treatment Relieves the Dysfunction of the Mitochondrial Respiratory Chain

(A) The complex I activities of various tissues. (B) The activities of complexes II+III. (C) Complex IV activities of various tissues. Mitochondria were isolated from different high energy consumption tissues (brain, heart, liver, and muscle) from 4-month-old male mice (n = 3 for each group).

in the cohort of our previous report and the work of others.[4–6] Six out of fourteen pediatric patients died prematurely in the cohort we reported. Thus, the severity of this syndrome is recognizable. More patients have since been verified to carry pathogenic *FDXR* mutations. Thus, an AAV vector that can deliver the rescuing gene globally, along with the CNS, is essential. Moreover, a vector that is capable of being administrated non-invasively is ideal, since the patients suffering from the mitochondrial syndrome are often at risk for complications associated with invasive procedures like craniotomy or intracranial catheter drainage. Additionally, general anesthesia could also be perilous for these patients.[24] The tropism of serotypes such as AAV-PHP.B toward the CNS and the ubiquitous expression profile of the CMV promoter could be advantageous for the disorders of FDXR mutation under these circumstances. Since the severe cases with FDXR mutation could be prematurely lethal, we administered the AAV-*Fdxr* vector to neonatal *Fdxr*$^{R389Q/R389Q}$ mutant mice (i.e., by P2) in an attempt to realize an early intervention. Western blot (WB) analysis in 5-month-old subjects revealed long term expression could be achieved via neonatal administration (Figure 1). IF staining 2 weeks after the delivery procedure also verified the excellent transduction efficiency of our AAV vector over the entire body, as shown in Figure 1.

Optic atrophy, sensory neuropathy, hind limb paralysis, movement disorders, and mitochondrial respiratory chain dysfunctions are the critical features of *FDXR* mitochondrial neuropathy.[4,5] Therefore, it is essential to ensure that our gene therapy strategy has addressed these pathological changes after the treatment. Significant improvements were observed *in vivo*; the optic atrophy and the demyelination of sciatic nerves were restored in treated subjects (Figures 3 and 4), and behavioral tests showed that the mutants could move without any issue after the AAV-*Fdxr* treatment, along with substantial improvements in both acoustic sensitivity and tactile sensory ability (Figure 7). Even more promising was the significant increase in cognitive and memory function in the treated *Fdxr*$^{R389Q/R389Q}$ mutant mice when they were tested using the MWM. The MWM also demonstrated that there was an improvement in the visual acuity of the treated animals since this test requires that the subjects possess sufficient function of the optic system to seek the escape path from the maze. Combined with the results of IF staining and EM, we believe that the improvement of these pathological phenotypes is related to the mitigation of the chronic inflammation and glial hyperplasia in the CNS, the decrease of degenerative lesions in cerebellum neurons, and the improvement of the optic nerve and the corresponding reduction in RGC loss. Gene therapy also improved the energy supply in these tissues, as well as the activity of mitochondrial respiratory chain complexes, particularly in the brain, heart, and muscle tissues. One

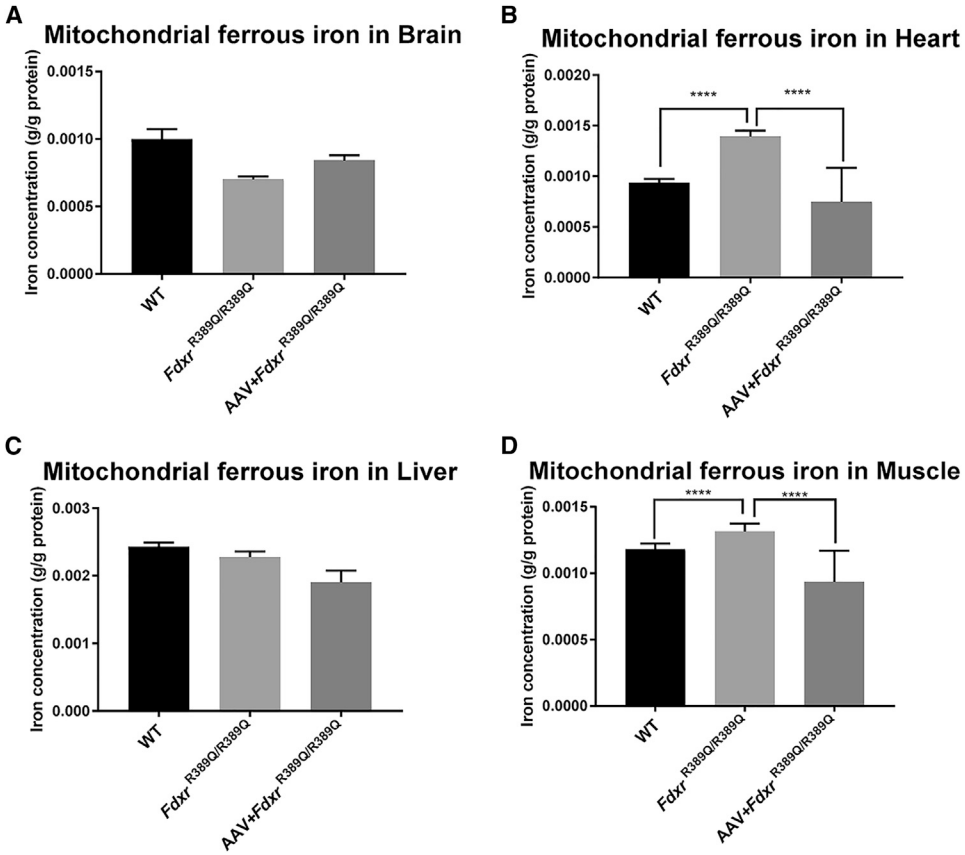

Figure 6. The AAV-*Fdxr* Treatment Eliminates the Mitochondrial Iron Overload in Various Tissues of *Fdxr*$^{R389Q/R389Q}$ Mutants

Levels of mitochondrial iron content were measured using colorimetric methods. (A–D) Mitochondria were isolated from energy-intensive tissues such as the brain (A), heart (B), liver (C), and muscle (D) from 4-month-old male mice (n = 3 for each group).

underlying reason for FDXR-mediated neurodegeneration may be that neurons containing long axons, such as those found in the CNS and the retina, require a great deal of energy to grow, extend, and maintain those axons. Thus, the demonstrable improvement in cellular energy supply that comes with the restoration of FDXR function by the viral vector may be helping to preserve these neurons simply by helping them regain some of that valuable energy production capacity. Replacement of FDXR function also appears to aid in the preservation of myelin, which is required to maintain rapid neural conduction. Thus, it appears likely that the normal function of these energy-intensive tissues is precisely the key to maintaining advanced nerve activity, the proper blood supply in tissues, and normal somatic motor function.

Some unrevealed phenotypes of FDXR-related mitochondrial neuropathy have been uncovered in this study. Since the adrenal gland is generally thought to have the highest FDXR protein expression in mouse tissues, we investigated the expression level of FDXR in this tissue within both mouse groups. Interestingly, we found that the FDXR protein level decreased significantly in the adrenal gland tissue lysates (Figure 1). Furthermore, the FDXR loss in the adrenal glands was restored to some extent after our gene therapy (Figure 1). Moreover, this protein decrease was not evidenced in the brain tissue. However, as the expression level of FDXR in the brain was almost equal between WT animals and *Fdxr*$^{R389Q/R389Q}$ mutants, the AAV-*Fdxr* therapy did not lead to Fdxr overexpression in the brain tissues. This phenomenon might indicate that the therapeutic transgenic product that we injected (*Fdxr* cDNA in this case) has been regulated at the translational level to maintain healthy levels of the FDXR protein, rather than translated randomly without any regulation from the host. Therefore, we explored the FDXR expression level in the liver tissues of 5-month-old mice, to investigate the expression pattern in another peripheral tissue. This analysis showed that the FDXR expression in the liver was increased after AAV treatment, which is the same pattern as the adrenal gland. However, the exact transduction pattern after the AAV treatment procedure still requires further investigation.

We also investigated the iron concentration in the 5-month-old *Fdxr*$^{R389Q/R389Q}$ mutants, given that FDXR is the first unit in the cytosolic Fe-S cluster assembly. As expected, the colorimetric assay of ferric iron levels showed that the *Fdxr*$^{R389Q/R389Q}$ mutants suffered iron overload in both heart and muscle tissues (Figure 6). Consistent

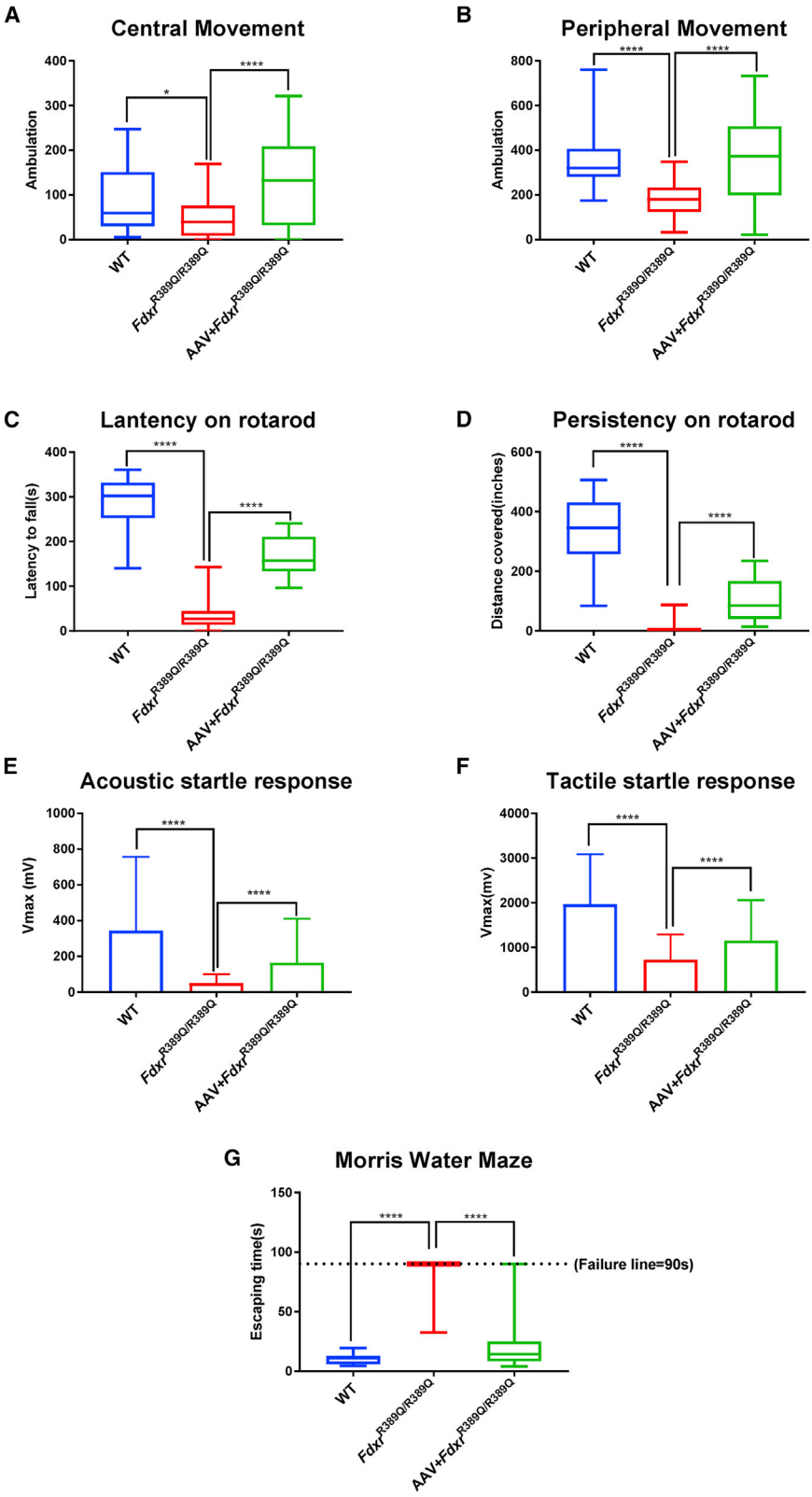

Figure 7. AAV-*Fdxr* Recovered the Movement Disorder and Sensory Defect of *Fdxr*$^{R389Q/R389Q}$ Mutants

Behavioral tests of 5-month-old female mice. (A) Movement frequency in the central area of locomotor activity chambers for 5-month-old female mice. (B) Motion recording in the peripheral areas of the locomotor chambers. (C) Lantency on rotarod and (D) Persistency on rotarod for 5-month-old female mice (n = 5 for each group). (E) Acoustic and startle response and (F) tactile startle response of 5-month-old female mice. (n = 5 for each group). (G) MWM performance of 5-month-old mice. A total assay time over 90 s indicates a failure to escape from the water maze (n = 5 for each group).

with this observation, the heart and muscle were also the most affected tissues in assays of mitochondrial respiratory dysfunction (Figure 5), which may help explain the movement difficulties of *Fdxr*$^{R389Q/R389Q}$ mutants at 2 months of age. Nevertheless, the exact mechanism behind those phenotypes still requires additional exploration.

In summary, we present the first demonstration of a potentially definitive treatment that significantly improves optic and sciatic nerve atrophy, sensory neuropathy, and mitochondrial dysfunction in *FDXR*-related mitochondriopathy. This study is among the first set of gene therapy studies of systematic mitochondrial syndrome using AAV vectors via a non-invasive procedure.[25–29] The early administrations of the therapeutic AAV-Fdxr vector maintained a substantial expression improvement over time, even at 5 months post-administration. Importantly, no visible adverse effects were observed in any of the mice exposed to this therapeutic strategy. As a variety of AAV-mediated gene delivery strategies are currently undergoing evaluation to determine their clinical efficacy in treating a spectrum of genetically inherited disorders in humans, a strong precedent exists for our strategy to be successfully introduced as an efficient therapy for inherited mitochondrial diseases. Thus, our study provides substantial support for the translation of AAV-*Fdxr* gene therapy into clinical utilization for the treatment of *FDXR*-related mitochondriopathy and optic atrophy.

MATERIALS AND METHODS

Animal Husbandry and Mouse Strains

The mouse strain utilized for this study is B6/129 S-*Fdxr*^{m1J} *Otop3*^{m1J}/GrsrJ (The Jackson Laboratory, Stock #026096). The mice were obtained from the Jackson Laboratory and raised inside the animal barrier of Cincinnati Children's Hospital Medical Center (CCHMC). The mice were maintained on a 12 h dark/light cycle, and all mice were fed *ad libitum*. These mice also carry a homozygous variant with an uncertain clinical significance in the 5′ untranslated region of *Otop3*. Mutation of the *Otop3* gene results in increased startle reflex and oligodactyly (MGI: 5450617), which is unlikely to contribute to the phenotype according to the previous study.[4] All animal procedures were performed in accordance with the Institutional Animal Care and Use Committee (IACUC)-approved protocol of CCHMC.

AAV Vector Production

The AAV vector carrying the *Fdxr* CDS (MGI: 104724) was designed as shown in Figure S1. The *Fdxr* CDS was acquired from a plasmid carrying the full-length *Fdxr* cDNA (clone ID: 14149, purchased from Dharmacon, Lafayette, CO, USA). The *Fdxr* CDS was then subcloned into the AAV vector pAV-FH (Vigene Biosciences, Rockville, MD, USA) upstream of an in-frame FLAG tag and under the control of a CMV promoter. The vector also contains an eGFP reporter downstream of the FLAG tag and separated by a P2A self-cleaving peptide. The resulting AAV viral vector enclosing *Fdxr* cDNA was cross-packaged as serotype PHP.B to facilitate transduction globally *in vivo*, including the CNS. The packaging, purification, and titration of the reassembled viral vector were carried out by Vigene Biosciences (Rockville, MD, USA). Purified vectors were stored in 1× PBS containing 350 mM NaCl and 5% D-sorbitol. AAV-PHP.B eGFP virus was utilized as a negative control for untreated *Fdxr*$^{R389Q/R389Q}$ mutants.

Systematic AAV Vector Delivery

Aliquots of the vector were injected into the temporal facial vein of neonatal mice according to a previously described protocol.[30] Briefly, P1 to P2 mice were immobilized with freezing anesthesia on wet ice for 30–60 s. An aliquot of the viral vector to be injected was thawed out at the same time, at doses of 2×10^{11} genome copies (GC)/g, diluted in 20 uL PBS. The pups were considered under deep anesthesia when they showed a state of decreased activity while still maintaining a smooth rate of breathing. After deep anesthesia was confirmed, the mice were placed under an anatomical microscope. An insulin syringe with a 31-gauge needle (BD, USA), containing an aliquot of the AAV vector was inserted into the temporal vein. Once the content of the syringe was injected into the facial vein, the lower facial vein showed signs of whitening. The needle was retracted afterward, and the site of injection was pressed with a cotton stick until the blood was clotted. Pups were then warmed with a heat pack to recover from low body temperature and placed back with the dam.

Mouse Behavioral Tests

Mouse behavioral tests were all conducted at the Center for Animal Behavior Studies, Department of Neurology, CCHMC.

Rotarod Test

We placed the 3 groups of 5-month-old mice on a Rotarod (UGO Basile Accelerating Rotarod, USA) with an accelerating rotating device and gradually increased the rotation speed of the Rotarod from 4 rpm to 40 rpm. The length of time that each mouse was able to remain on the Rotarod before falling and the total distance traveled by each mouse was recorded, and the differences between the groups were compared.

Mouse Activity Test

Mouse activity tests were carried out in an independent 41 × 41 × 30 cm cubic monitor box (Accuscan Electronics with VersaMax Software, USA) for each subject. The monitor box is equipped with 16 LED beams along the x and y axes. Each surveillance box is equipped with fluorescent lights similar to those in the living environment of the subjects. 5-month-old mice were placed in a monitoring box for 60 min. The total frequency of motions and fine-movements of the subjects were recorded at 5-min intervals, and the differences between groups were compared.

MWM Test

The MWM test was carried out as previously described.[31] Briefly, the test animals were placed in an open, circular pool with a submerged platform. The test animals were trained to swim to the platform from various locations or to try to find the platform after it had been removed. The escape time from the water maze was measured for

each subject, and comparisons of each group were conducted after the test. Any mouse incapable of escaping from the water maze within 90 s was considered as a failure to escape, and the animal was then rescued from the water maze.

Startle Tests

Acoustic startle response was assessed as previously described.[32] In short, a white noise background of 70 dB, a prepulse of 73, 77, and 82 dB, and a mixed frequency startle stimulus of 120 dB (as the unexpected stimulus) were used in the acoustic assay. In a tactile startle assay, animals were exposed to a disruptive air puff, and the degree of the animal response was recorded by an electrode placed provisionally in the ears of the subjects. The amplitudes obtained from the subjects in each group after each pulse of the stimulus were compared.

H&E Staining

Eyes were fixed in 4% PFA for 24 h at room temperature and then embedded in paraffin. Sagittal sections of the eye (8 μm) were cut through the optic nerve head. Slides were then deparaffinized using a xylene-gradient ethanol procedure, followed by staining with hematoxylin and counterstaining with eosin. Slides were then mounted using DPX mounting medium (Sigma-Aldrich, MO, USA). Images were obtained under light microscopy (BX63; Olympus Corporation; Center Valley, PA, USA). Nuclei in the RGC layer (excluding the small and flat nuclei of the endothelial cells) were counted using an ImageJ program.

Transmission EM (TEM) and Toluidine Blue Staining

4-month-old male mice were anesthetized using CO_2 and perfused with 0.9% saline; then, the tissues were isolated and transferred into the EM fixative (4% paraformaldehyde [PFA], 2.5% glutaraldehyde, PBS, pH 7.4–7.6). Tissues were postfixed in EM fixative for 24 h, followed by rinsing in 0.1 M Na cacodylate buffer (EMS, Hatfield, PA, USA), and finally postfixed in 1% osmium tetroxide (EMS) for 1 h at 4°C. Rinsed tissues were then washed in 0.1 M Na cacodylate buffer and dehydrated through a gradient concentration of ethanol. Samples were then embedded in LX-112 resin (Ladd Research Industries, Williston, VT, USA). Afterward, tissue blocks were cut into a thickness of 0.5 μm and stained with toluidine blue for observation under a bright-field microscope. For TEM, tissue blocks were sectioned and trimmed with an ultramicrotome (Leica EM UC7, Buffalo Grove, IL, USA) to a thickness of 90 nm. Sections were counterstained with uranyl acetate 2% (EMS) and lead citrate. All TEM images were acquired from an 80-kV transmission electron microscope (Hitachi, H-7650, V01.07, Tokyo, Japan).

IF Staining

Frozen tissue sections of 5-month-old mice were processed as previously reported.[33] Briefly, mice were perfused transcardially with ice-cold PBS, then by 4% PFA. After perfusion, tissues were postfixed in 4% PFA at 4°C, then dehydrated in 30% sucrose for 24 h. Mouse tissues were cut on a LEICA CM1850 cryostat (Leica, Germany) into 10 μm thickness sections, then transferred onto SuperFrost microscope slides (Thermo Fisher Scientific, NH, USA) for IF staining. Mouse tissue sections were labeled with the following primary antibodies: mouse anti-GFAP (1:1,000, Millipore, MA, USA, IF03L), and mouse anti-Brn-3a (1:250, Santa Cruz, TX, USA, sc-8429). Donkey anti-rabbit Alexa Fluor 488 (1:500, Jackson ImmunoResearch, AB_2313584) and donkey anti-rabbit Alexa Fluor 594 (Invitrogen, R37119) were utilized as the secondary antibodies. A mounting medium including 4′,6-diamidino-2-phenylindole (DAPI; Vector, CA, USA) was used as a counterstain for the nucleus. Stained slides were imaged with a Nikon C2 confocal microscope (Nikon, Japan).

Fluoro-Jade C Staining

4-month-old mouse brain tissues were first embedded in paraffin, and then trimmed and cut into 5 μm thickness sections before being mounted on SuperFrost microscope slides (Thermo Fisher Scientific, NH, USA). Afterward, tissue sections were deparaffinized and rehydrated under a gradient xylene-ethanol procedure. First, slides were immersed in 1% NaOH diluted in 80% ethanol for 2 min, then rinsed in 70% ethanol for 2 min, followed by distilled water-rinsing for another 2 min. After the rinse, the slides were incubated in 0.06% potassium permanganate for 10 min. Following another 2-min rinse in water, slides were then transferred into a solution containing 0.0001% Fluoro-Jade C in 0.1% acetic acid and then incubated for another 10 min. After washing three times with water (2 min per wash), slides were dried in an incubator at 50°C for 30 min, then coverslipped with DPX mounting medium (Sigma-Aldrich, MO, USA) after being cleared in xylene. Signals were visualized using a Nikon C2 confocal fluorescence microscope.

WB

The WB process was carried out as previously described.[4] Tissues from 4-month-old female mice were collected after euthanasia and then homogenized to generate cell lysates. 60 μg of protein isolated from each tissue was mixed with 2X radioimmunoprecipitation assay (RIPA) lysis and extraction buffer (Thermo Fisher Scientific, NH, USA). Then, the mingled samples were denatured for 5 min at 95°C before running on a NuPAGE 10% Bis-Tris gel (Invitrogen, Carlsbad, CA, USA). The gel was then transferred afterward onto a polyvinylidene fluoride (PVDF) membrane using an iBlot semi-dry transferring system (Invitrogen, Carlsbad, CA, USA). Later, the PVDF membrane was blocked in intercept blocking buffer (LI-COR Biosciences, Lincoln, NE, USA) for 45 min and then incubated overnight with primary antibodies diluted in blocking buffer with 0.1% Tween 20 and rabbit anti-FDXR (Abcam ab204310) at 1:200 dilution. Rabbit anti-GAPDH (Glyceraldehyde 3-phosphate dehydrogenase) (Ambion, AM4300, Foster City, CA, USA) at 1:2,000 dilution and mouse anti-beta-actin (Invitrogen, MA1-140, Carlsbad, CA, USA) at 1:5,000 dilution were used as internal controls. After overnight incubation, the membrane was washed three times (10 min per wash), then incubated for 90 min with IRDye 680RD goat anti-rabbit immunoglobulin G (IgG) secondary antibody (LI-COR Biosciences, Lincoln, NE, USA). Protein bands were visualized and quantified using the LI-COR Odyssey Clx Imaging System (LI-COR Biosciences, Lincoln, NE, USA).

Mitochondrial Complex Activity Assays

The relative activity of mitochondrial respiratory chain complexes was measured as previously reported.[34] In short, mitochondrial complex I activity was determined by measuring the descending NADH absorbance at 340 nm, with decylubiquinone used as an electron acceptor. Complex II and III activity levels were assessed by the inclining absorbance of reduced cytochrome C at 550 nm; potassium cyanide was utilized in the medium to inhibit the subsequent oxidation. Complex IV activity was determined using the Complex IV Rodent Enzyme Activity Microplate Assay Kit (Abcam, United Kingdom). The activity of complex IV was measured by testing the oxidation of reduced cytochrome *c*, which was determined by monitoring the dynamic of absorbance at 550 nm. All absorbance values of the mitochondrial complex assays were recorded using a Synergy H1 microplate reader (Biotek Instruments, VT, USA). The relative enzymatic activity was calculated as nmol/min/mg protein and normalized to the value of WT mice.

Mitochondrial Iron Concentration Detection

Mitochondrial iron concentration assay was carried out with the MAK025 iron content detection kit (Sigma-Aldrich, USA) according to the user manual. Briefly, the mitochondria of each mouse tissue were first isolated following a gradient centrifugation protocol, as previously described.[35] After a gradient iron standard system was established, 50 μL of mitochondrial protein was then added into each sampling well, and then 50 μL of working buffer was added into each well. Next, 5 μL of the iron detector was added to both the sample wells and the standard wells to determine the content of ferrous iron (Fe^{2+}). Samples were then incubated at room temperature for 30 min, avoiding light. After incubation, 100 μL of the iron probe was added to each sample and standard well, and the whole system was incubated at RT for another 60 min in the dark. Finally, the absorbance values at 593 nm of each sample were read on the Synergy H1 microplate reader. The iron concentration (C) of each sample was calculated according to the following formula: C = Sa/Sv. (Sa, nmol of the sample on the standard curve; Sv, the total volume of the sample).

EMG Recording

EMG was carried out as previously described.[36] 4-month-old male mice were anesthetized with isoflurane inhalation, followed by 50 mg/kg sodium phenobarbital intraperitoneal injection. Afterward, the lateral gastrocnemius muscle of the mice was exposed from the knee to approximately 4 mm above the ankle. Then, the sciatic nerve was exposed near the biceps femoris. We implanted a polyester film wrap line (California thin line) on the outside of the mouse gastrocnemius and inserted a reference line below the skin near the tail of the mouse. We placed a concentric bipolar stimulation electrode on the sciatic nerve of the mouse for electrical activation. The composite muscle action potential (CMAP) was amplified and acquired using a Micro 1401 data acquisition unit and analyzed offline using Spike5 software (Cambridge Electronic Design, Cambridge, UK). The sciatic nerve adjacent to the tibia and fibula received 2–4 mA electrical stimulation through a stimulating isolator (World Precision Instruments, Sarasota, FL) attached to a Micro 1401 data acquisition unit. After the data recording was complete, the sciatic nerve axons were removed, and the proximal sciatic nerve was stimulated to ensure direct neural stimulation produces CMAP. We calculated CMAP and CV according to each stimulation module. Then the average stimulation size of the sciatic nerve under each module was recorded and averaged in each animal.

Statistical Analysis

The comparisons between groups were made using one-way ANOVA, followed by Dunnett post hoc tests. Graphical illustrations and significance were obtained with GraphPad Prism 7 (GraphPad). $p < 0.05$ was considered statistically significant (*$p < 0.05$; **$p < 0.01$; ***$p < 0.001$; ****$p < 0.0001$).

SUPPLEMENTAL INFORMATION

Supplemental Information can be found online at https://doi.org/10.1016/j.omtm.2020.05.021.

AUTHOR CONTRIBUTIONS

L.Y., J.S., F.Y., and T.H. conceived the idea; L.Y., J.S., W.Z., L.F.Q., and M.P.J. performed experiments; L.Y. collected data; L.Y., J.S., and W.Z. analyzed data; L.Y, J.S., and T.H. wrote the manuscript. The project was designed and supervised by T.H.

CONFLICTS OF INTEREST

The authors declare no competing interests.

ACKNOWLEDGMENTS

This work was supported by the Center for Pediatric Genomics (CpG), with funding from Cincinnati Children's Research Foundation and National Institutes of Health (1R01EY026609-01) to T.H. The EMG recordings were partially supported by a National Institutes of Health grant (R01AR064551-01A1) to M.P.J. L.Y. is the recipient of the studying abroad grants program of the China Scholarship Council. The funders had no role in study design, data collection and analysis, decision to publish, or preparation of the manuscript. We appreciate the help of Dr. Charles Vorhees' Lab at CCHMC in conducting the behavioral tests and the data analysis of those results.

REFERENCES

1. Hanukoglu, I. (1992). Steroidogenic enzymes: structure, function, and role in regulation of steroid hormone biosynthesis. J. Steroid Biochem. Mol. Biol. *43*, 779–804.

2. Shi, Y., Ghosh, M., Kovtunovych, G., Crooks, D.R., and Rouault, T.A. (2012). Both human ferredoxins 1 and 2 and ferredoxin reductase are important for iron-sulfur cluster biogenesis. Biochim. Biophys. Acta *1823*, 484–492.

3. Solish, S.B., Picado-Leonard, J., Morel, Y., Kuhn, R.W., Mohandas, T.K., Hanukoglu, I., and Miller, W.L. (1988). Human adrenodoxin reductase: two mRNAs encoded by a single gene on chromosome 17cen——q25 are expressed in steroidogenic tissues. Proc. Natl. Acad. Sci. USA *85*, 7104–7108.

4. Peng, Y., Shinde, D.N., Valencia, C.A., Mo, J.S., Rosenfeld, J., Truitt Cho, M., Chamberlin, A., Li, Z., Liu, J., Gui, B., et al. (2017). Biallelic mutations in the ferredoxin reductase gene cause novel mitochondriopathy with optic atrophy. Hum. Mol. Genet. *26*, 4937–4950.

5. Paul, A., Drecourt, A., Petit, F., Deguine, D.D., Vasnier, C., Oufadem, M., Masson, C., Bonnet, C., Masmoudi, S., Mosnier, I., et al. (2017). FDXR Mutations Cause Sensorial

Neuropathies and Expand the Spectrum of Mitochondrial Fe-S-Synthesis Diseases. Am. J. Hum. Genet. *101*, 630–637.

6. Slone, J., Peng, Y., Chamberlin, A., Harris, B., Kaylor, J., McDonald, M.T., Lemmon, M., El-Dairi, M.A., Tchapyjnikov, D., Gonzalez-Krellwitz, L.A., et al. (2018). Biallelic mutations in FDXR cause neurodegeneration associated with inflammation. J. Hum. Genet. *63*, 1211–1222.
7. Slone, J., Gui, B., and Huang, T. (2018). The current landscape for the treatment of mitochondrial disorders. J. Genet. Genomics *45*, 71–77.
8. Parikh, S., Saneto, R., Falk, M.J., Anselm, I., Cohen, B.H., Haas, R., and Medicine Society, T.M. (2009). A modern approach to the treatment of mitochondrial disease. Curr. Treat. Options Neurol. *11*, 414–430.
9. Avula, S., Parikh, S., Demarest, S., Kurz, J., and Gropman, A. (2014). Treatment of mitochondrial disorders. Curr. Treat. Options Neurol. *16*, 292.
10. Naso, M.F., Tomkowicz, B., Perry, W.L., 3rd, and Strohl, W.R. (2017). Adeno-Associated Virus (AAV) as a Vector for Gene Therapy. BioDrugs *31*, 317–334.
11. Deverman, B.E., Ravina, B.M., Bankiewicz, K.S., Paul, S.M., and Sah, D.W.Y. (2018). Gene therapy for neurological disorders: progress and prospects. Nat. Rev. Drug Discov. *17*, 641–659.
12. Morabito, G., Giannelli, S.G., Ordazzo, G., Bido, S., Castoldi, V., Indrigo, M., Cabassi, T., Cattaneo, S., Luoni, M., Cancellieri, C., et al. (2017). AAV-PHP.B-Mediated Global-Scale Expression in the Mouse Nervous System Enables GBA1 Gene Therapy for Wide Protection from Synucleinopathy. Mol. Ther *25*, 2727–2742.
13. Chan, K.Y., Jang, M.J., Yoo, B.B., Greenbaum, A., Ravi, N., Wu, W.L., Sánchez-Guardado, L., Lois, C., Mazmanian, S.K., Deverman, B.E., and Gradinaru, V. (2017). Engineered AAVs for efficient noninvasive gene delivery to the central and peripheral nervous systems. Nat. Neurosci. *20*, 1172–1179.
14. Itoh, S., Iemura, O., Yamada, E., Yoshimura, T., Tsujikawa, K., Kohama, Y., and Mimura, T. (1995). cDNA cloning of mouse ferredoxin reductase from kidney. Biochim. Biophys. Acta *1264*, 159–162.
15. Zhang, Y., Qian, Y., Zhang, J., Yan, W., Jung, Y.S., Chen, M., Huang, E., Lloyd, K., Duan, Y., Wang, J., et al. (2017). Ferredoxin reductase is critical for p53-dependent tumor suppression via iron regulatory protein 2. Genes Dev. *31*, 1243–1256.
16. Chinnery, P.F., and Turnbull, D.M. (2001). Epidemiology and treatment of mitochondrial disorders. Am. J. Med. Genet. *106*, 94–101.
17. Dimauro, S., Mancuso, M., and Naini, A. (2004). Mitochondrial encephalomyopathies: therapeutic approach. Ann. N Y Acad. Sci. *1011*, 232–245.
18. DiMauro, S., Hirano, M., and Schon, E.A. (2006). Approaches to the treatment of mitochondrial diseases. Muscle Nerve *34*, 265–283.
19. Tarnopolsky, M.A. (2008). The mitochondrial cocktail: rationale for combined nutraceutical therapy in mitochondrial cytopathies. Adv. Drug Deliv. Rev. *60*, 1561–1567.
20. Calvo, S.E., Clauser, K.R., and Mootha, V.K. (2016). MitoCarta2.0: an updated inventory of mammalian mitochondrial proteins. Nucleic Acids Res. *44* (D1), D1251–D1257.
21. Mayr, J.A., Haack, T.B., Freisinger, P., Karall, D., Makowski, C., Koch, J., Feichtinger, R.G., Zimmermann, F.A., Rolinski, B., Ahting, U., et al. (2015). Spectrum of combined respiratory chain defects. J. Inherit. Metab. Dis. *38*, 629–640.
22. DiMauro, S., and Schon, E.A. (2003). Mitochondrial respiratory-chain diseases. N. Engl. J. Med. *348*, 2656–2668.
23. Gorman, G.S., Schaefer, A.M., Ng, Y., Gomez, N., Blakely, E.L., Alston, C.L., Feeney, C., Horvath, R., Yu-Wai-Man, P., Chinnery, P.F., et al. (2015). Prevalence of nuclear and mitochondrial DNA mutations related to adult mitochondrial disease. Ann. Neurol. *77*, 753–759.
24. Niezgoda, J., and Morgan, P.G. (2013). Anesthetic considerations in patients with mitochondrial defects. Paediatr. Anaesth. *23*, 785–793.
25. Cabrera-Pérez, R., Vila-Julià, F., Hirano, M., Mingozzi, F., Torres-Torronteras, J., and Martí, R. (2019). Alpha-1-Antitrypsin Promoter Improves the Efficacy of an Adeno-Associated Virus Vector for the Treatment of Mitochondrial Neurogastrointestinal Encephalomyopathy. Hum. Gene Ther. *30*, 985–998.
26. Suzuki-Hatano, S., Saha, M., Rizzo, S.A., Witko, R.L., Gosiker, B.J., Ramanathan, M., Soustek, M.S., Jones, M.D., Kang, P.B., Byrne, B.J., et al. (2019). AAV-Mediated TAZ Gene Replacement Restores Mitochondrial and Cardioskeletal Function in Barth Syndrome. Hum. Gene Ther. *30*, 139–154.
27. Di Meo, I., Marchet, S., Lamperti, C., Zeviani, M., and Viscomi, C. (2017). AAV9-based gene therapy partially ameliorates the clinical phenotype of a mouse model of Leigh syndrome. Gene Ther. *24*, 661–667.
28. Cwerman-Thibault, H., Augustin, S., Ellouze, S., Sahel, J.A., and Corral-Debrinski, M. (2014). Gene therapy for mitochondrial diseases: Leber Hereditary Optic Neuropathy as the first candidate for a clinical trial. C. R. Biol. *337*, 193–206.
29. Torres-Torronteras, J., Viscomi, C., Cabrera-Perez, R., Camara, Y., Di Meo, I., Barquinero, J., Auricchio, A., Pizzorno, G., Hirano, M., et al. (2014). Gene therapy using a liver-targeted AAV vector restores nucleoside and nucleotide homeostasis in a murine model of MNGIE. Mol. Ther *22*, 901–907.
30. Gombash Lampe, S.E., Kaspar, B.K., and Foust, K.D. (2014). Intravenous injections in neonatal mice. J. Vis. Exp. *11*, e52037.
31. Vorhees, C.V., and Williams, M.T. (2006). Morris water maze: procedures for assessing spatial and related forms of learning and memory. Nat. Protoc. *1*, 848–858.
32. Vorhees, C.V., Morford, L.R., Graham, D.L., Skelton, M.R., and Williams, M.T. (2011). Effects of periadolescent fluoxetine and paroxetine on elevated plus-maze, acoustic startle, and swimming immobility in rats while on and off-drug. Behav. Brain Funct. *7*, 41.
33. Riazifar, H., Sun, G., Wang, X., Rupp, A., Vemaraju, S., Ross-Cisneros, F.N., Lang, R.A., Sadun, A.A., Hattar, S., Guan, M.X., and Huang, T. (2015). Phenotypic and functional characterization of Bst+/- mouse retina. Dis. Model. Mech. *8*, 969–976.
34. Simon, M., Richard, E.M., Wang, X., Shahzad, M., Huang, V.H., Qaiser, T.A., Potluri, P., Mahl, S.E., Davila, A., Nazli, S., et al. (2015). Mutations of human NARS2, encoding the mitochondrial asparaginyl-tRNA synthetase, cause nonsyndromic deafness and Leigh syndrome. PLoS Genet. *11*, e1005097.
35. Graham, J.M. (2001). Purification of a crude mitochondrial fraction by density-gradient centrifugation. Curr. Protoc. Cell Biol *4*, 1–22.
36. Li, Z., Peng, Y., Hufnagel, R.B., Hu, Y.C., Zhao, C., Queme, L.F., Khuchua, Z., Driver, A.M., Dong, F., Lu, Q.R., et al. (2017). Loss of SLC25A46 causes neurodegeneration by affecting mitochondrial dynamics and energy production in mice. Hum. Mol. Genet. *26*, 3776–3791.